



Effect of Variable Outlets on the Nonreactive Flowfield of a Right-Cylindrical Cyclonic Chamber

Gaurav Sharma* and Joseph Majdalani†

Auburn University, Auburn, AL 36849

This work focuses on the use of a finite-volume solver to describe the wall-bounded cyclonic flowfield that evolves in a swirl-driven thrust chamber. More specifically, a non-reactive, cold-flow simulation is carried out using an idealized chamber configuration of a square-shaped, right-cylindrical enclosure with eight tangential injectors and a variable nozzle size. For simplicity, we opt for air as the working fluid and perform our simulations under steady, incompressible, and inviscid flow conditions. First, a meticulously developed mesh that consists of tetrahedral elements is generated in a manner to minimize the overall skewness, especially near injectors; second, this mesh is converted into a polyhedral grid to improve convergence characteristics and accuracy. After achieving convergence in all variables, our three velocity components are examined and compared to an existing analytical solution obtained by Vyas and Majdalani (Vyas, A. B., and Majdalani, J., "Exact Solution of the Bidirectional Vortex," *AIAA Journal*, Vol. 44, No. 10, 2006, pp. 2208-2216). We find that the numerical model is capable of predicting the expected forced vortex behavior in the inner core region as well as the free vortex tail in the inviscid region. Moreover, the results appear to be in fair agreement with the Vyas-Majdalani solution derived under similarly inviscid conditions, and thus resulting in a quasi complex-lamellar profile. In this work, we are able to ascertain the axial independence of the swirl velocity no matter the value of the outlet radius, which confirms the key assumption made in most analytical models of wall-bounded cyclonic motions. Moreover, the pressure distribution predicted numerically is found to be in fair agreement with both theoretical formulations and experimental measurements of cyclone separators. The bidirectional character of the flowfield is also corroborated by the axial and radial velocity distributions, which are found to be concurrent with theory. Then using parametric trade studies, the sensitivity of the numerical simulations to the outlet diameter of the chamber is explored to determine the influence of outlet nozzle variations on the mantle location and the number of mantles. Since none of the cases considered here promote the onset of multiple mantles, we are led to believe that more factors are involved in producing more mantles than one. Besides the exit diameter, the formation of a multiple mantle structure may be influenced by the physical boundary conditions, nozzle radius, inlet curvature, and length. In closing, we show that the latter plays a significant role in controlling the development of backflow regions inside the chamber.

Nomenclature

A_{inj}	total injection area
A_{port}	port area of individual injector
D	chamber diameter
F	external body force
g	gravity
I	unit tensor
L	chamber length
N_{inj}	number of injectors
p	normalized pressure
P	static pressure
r	radial coordinate
\mathbf{u}	velocity of the fluid
u_r	normalized radial velocity
u_θ	normalized swirl velocity
u_z	normalized axial velocity
V	vortex Reynolds number
z	axial coordinate

*Graduate Research Assistant, Department of Aerospace Engineering, Member AIAA.

†Professor and Francis Chair, Department of Aerospace Engineering, Assoc. Fellow AIAA.

Greek

β	normalized discharge radius
μ, ρ	fluid molecular viscosity and density
$\bar{\tau}$	dimensional stress tensor

I. Introduction

THE characterization of wall-bounded cyclonic flows continues to receive attention in the propulsion community, and this is mainly due to the favorable attributes associated with the onset of rotating motion in vortex engines and other swirl-dominated thrust chambers [1]. By translating the basic characteristics of unconfined tornadoes and hurricanes to propulsive devices [2], researchers are able to leverage the high energy density, self-sustaining capability, self-cooling features, prolonged residence time, and effective mixing potential of cyclonic flows in efficient power production and thrust generation applications [3].

In principle, confined cyclonic flows can be classified as unidirectional, bidirectional, and multi-directional, depending on the number of longitudinal passes that a fluid entering the enclosure will undertake before exiting [4]. The primary emphasis of the present investigation will be on the bidirectional cyclonic pattern, which comprises two distinct swirling regions: the outer annular vortex, where the fluid spirals towards the headwall, and the inner vortex region, where the flow targets the endwall, or the base of the chamber. A discrete rotating but non-translating layer, known as the mantle, separates the two segments of the flow [5]. Swirl is sustained in accordance with the conservation of angular momentum of a tangentially injected fluid, which is often introduced near the endwall.

The earliest studies of bidirectional swirling flows may be traced back to ter Linden [6] and his experimental investigations of the geometric dimensions on the efficiency of cyclonic dust collectors. Then after four decades of sporadic studies, Bloor and Ingham [7] develop a simple incompressible model for wall-bounded conical cyclones from which they manage to extract a very useful closed-form solution. This is followed by a series of numerical simulations of confined cyclonic motions by Hsieh and Rajamani [8], Monredon et al. [9] and Hoekstra et al. [10]. In addition to their engagement in numerical investigations, some of these researchers also conduct experiments to validate their computational results. Later, by shifting attention back to the development of a viable mathematical framework for wall-bounded cylindrical and spherical cyclones, Vyas and Majdalani [5] and Majdalani and Rienstra [11] manage to produce exact inviscid solutions for the bulk cyclonic motion starting from first principles. However, to overcome the singularity that undermines the inviscid motion along its axis of rotation, Majdalani and Chiaverini [12] borrow the tools of boundary-layer theory to obtain viscous corrections that capture the forced vortex behavior in the core region of a bidirectional chamber. Along similar lines, Maicke and Majdalani [13] are able to overcome the inviscid singularity by implementing a constant shear stress model near the centerline. The necessity of securing the velocity adherence requirement near the sidewall is also investigated using matched-asymptotic expansions in a series of studies that lead to viscous approximations for the core and wall boundary layers [14–16]. Shortly thereafter, Majdalani [3] introduces several distinct families of helical motions of the “Beltramian” and “Trkalian” types that display rather compelling cyclonic flow patterns. Other complementary studies are pursued for the purpose of incorporating the effects of arbitrary headwall injection [17, 18], compressibility [19, 20], uniform sidewall injection [21, 22], and hollow cylindrical air cores [23].

Apart from the filtration industry, where dedusters and hydrocyclones are commonplace, several thrust chambers in the propulsion industry have been conceived to operate by leveraging the bidirectionality and swirl advantages of cyclones. Among those, two particular concepts come to mind, namely, the Vortex Injection Hybrid Rocket Engine (VIHRE), developed by Knuth et al. [24, 25], and the Vortex Combustion Cold-Wall Chamber (VCCWC), conceived by Chiaverini et al. [26]. For the reader’s convenience, schematics of the VIHRE and VCCWC concepts are furnished in Figs. 1a–1b. The VCCWC, which is more relevant to the central focus of this work, consists of a peculiar design where the oxidizer is injected tangentially from the endwall of the chamber just above the nozzle. After entering the chamber rather unconventionally, the oxidizer ascends along the walls in a spiraling motion that forms the “outer vortex” region. As it approaches the headwall, the oxidizer then turns inwardly, mixes with the fuel, and combusts vigorously, even as it heads down the centerline, where it is referred to as the “inner vortex” core. Through this helical trajectory, the outer annular vortex confines the reactants to the core region and prevents the hot products and gaseous mixtures from coming in contact with the walls. In practice, the resulting film cooling mechanism has been shown to be very effective at protecting the walls from the high convective and radiative core temperatures [1].

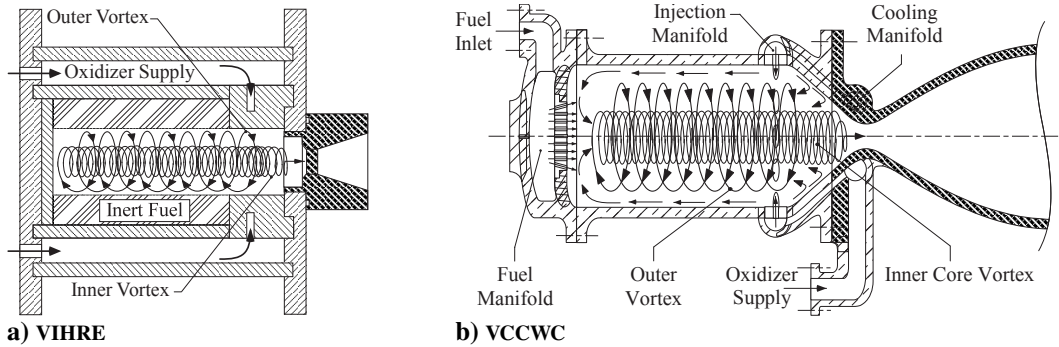


Fig. 1. Schematics of ORBITEC's a) Vortex Injection Hybrid Rocket Engine (VIHRE) conceived by Knuth et al. [24] and b) the Vortex Combustion Cold-Wall Chamber (VCCWC) developed by Chiaverini et al. [27].

It can be inferred from a perfunctory literature review that most of the experimental studies related to confined cyclonic motions have been carried out on cyclone separators or dust collectors. As such, most of the information pertaining to bidirectional vortex engines remains either limited or proprietary; few cases can be found including the cold-flow experimental and computational studies performed by Anderson et al. [28]. Their work considers a laboratory-scale model of a simplified cyclonic chamber and produces tangential velocity data at three specific axial locations using Particle Image Velocimetry (PIV). This PIV data is later used by Maicke and Majdalani [13, 29] to guide their viscous and constant shear stress formulations.

The use of numerical models in the treatment of cyclonic flows has continued to receive attention due to the evolution of hardware and affordability of resources relative to experimentation. In this vein, numerical simulations that describe wall-bounded cyclones have continued to appear and these have attempted different turbulence models in the hope of capturing the anisotropic behavior of the flow in the presence of a highly swirling environment. Despite these pursuits, investigations of precession, flow instability, and breakdown, which are susceptible to numerical simulations, have remained largely unattempted and unresolved. Moreover, the identification of appropriate turbulence models that are capable of handling highly anisotropic conditions continues to be an open question. In what follows, some of the pertinent efforts are briefly reviewed.

We begin with the design optimization study of Boysan et al. [30], where a two-phase algebraic turbulence model is constructed for gaseous cyclones with entrained solid particles. Their model computes six Reynolds stress components, thus leading to a numerical scheme that is capable of predicting grade-efficiency curves by means of stochastic particle tracking techniques. Nearly a decade later, another detailed study is conducted by Concha et al. [31], where different sets of equations are applied to each of six individual zones constituting a hydrocyclone. These equations are intended to permit the computation of local velocities with considerable precision. Then using the momentum balance of particle trajectories, the characteristic separation size is accurately deduced.

Along similar lines, Hoekstra et al. [10] carry out a comprehensive numerical investigation of cyclone separators with gas as the working fluid. Their study provides a comparison between different turbulence models and experimental results. Accordingly, the Reynolds stress transport model is found to be capable of producing more realistic predictions relative to other turbulence models. A year later, Derkzen and den Akker [32] extend this line of inquiry by using large eddy simulations (LES) to predict the fundamental features of a reverse-flow cyclone separator. Their study also discusses the precession patterns of the inner vortex and its stabilizing role. Advancing further in their investigation, Derkzen [33] applies this LES code to predict the separation performance of a high efficiency Stairmand-type cyclone using frozen-field, eddy-lifetime, and periodic-flow approaches. Derkzen et al. [34] also examine the effects of incorporating two-phase flow effects on the fidelity of their computations by successfully implementing two-way coupling. In the meantime, Hu et al. [35] modify the empirical constants for isotropization of their production and convection model (IPCM) as well as the wall-reflection term of their pressure-strain model to better handle anisotropic turbulence. This enables them to achieve an improved Reynolds stress model for strong swirling flows while dodging the computational costs associated with LES. By way of confirmation, their three-dimensional computations are shown to agree with measurements acquired in a cyclone separator using laser Doppler Velocimetry (LDV). In fact, this sequence of studies builds up to a comprehensive review by Cortes and Gil [36], where different computational models for reverse-flow cyclone separators are surveyed and cataloged based on their ability to predict the tangential velocity distribution, pressure drop, and collection efficiency.

Despite the existence of several numerical studies of cyclone separators, only few exist that devote themselves to the VCCWC flow configuration using, for instance, the laminar $k-\varepsilon$ and Reynolds stress transport (RSM) models. Among those, one may cite Fang and Majdalani [37], Anderson et al. [28], Murray et al. [38], Talamantes and Maicke [39], Sharma and Majdalani [40], Maicke and Talamantes [41], and Majdalani and Chiaverini [1]. In this work, we augment this line of inquiry by taking a close look at the cyclonic motion in an idealized VCCWC chamber using a robust finite-volume solver. Since most previous studies have mainly focused on the tangential velocity distribution, our emphasis here will be to perform cold-flow simulations that are capable of characterizing all three components of the velocity and pressure profiles while exploring the effects of the outlet radius and nozzle extension size on the positioning and formation of mantles and backflow regions.

II. Numerical Formulation

In previous work [40], the main objective was to compare numerical results to those of an exact complex-lamellar solution derived by Vyas and Majdalani [5] directly from Euler's equation. To do so, the geometry and boundary conditions in the numerical model were chosen as plainly as possible in order to mirror those associated with the theoretical framework. In view of the purely tangential injection assumed in the complex-lamellar model, special consideration had to be made to align the projected injectors in a similar arrangement along the outer circumference with no outward protrusions [40].

In the present work, we opt for a more realistic model, as depicted in Fig. 2, in order to reproduce a cyclonic motion that resembles the VCCWC flowfield more closely. To this end, a three-dimensional computational domain is conceived for an idealized depiction of the bidirectional vortex engine with eight protruding injectors. Our computational domain is protracted using SolidWorks with dimensions that are identical to those used by Anderson et al. [28]. It is subsequently meshed using a well-established meshing software (ICEM CFD). The discretized domain is then exported into our finite-volume solver, which is part of a commercially available multiphysics package, where an implicit, incompressible, Reynolds-averaged Navier-Stokes solver can be used [42]. The geometric details of the chamber and its injectors are provided in Table 1 and illustrated in Fig. 2. In the interest of clarity, Fig. 2a presents an isometric view of the idealized vortex chamber whereas Fig. 2b shows a side view that displays the actual dimensions used in the upcoming simulations.

A. Mesh Generation and Quasi-Inviscid Model

Creating a complete and effective structured mesh remains, perhaps, one of the most labor-intensive components of this study. The difficulty may be ascribed to the complications brought about by the need to carefully resolve and refine the mesh in the region surrounding the tangential injectors as well as the sidewall. For example, the small angle

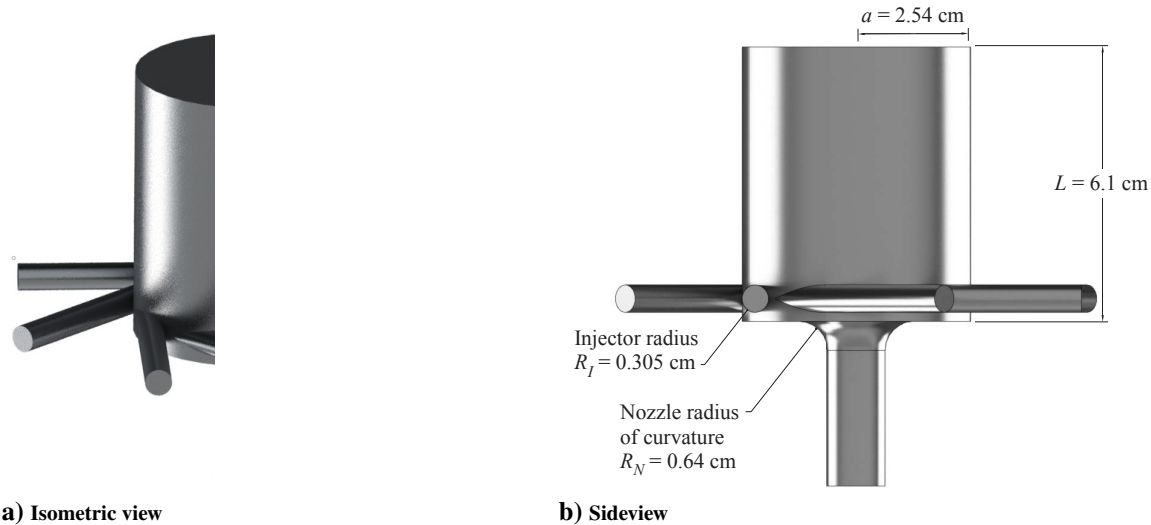
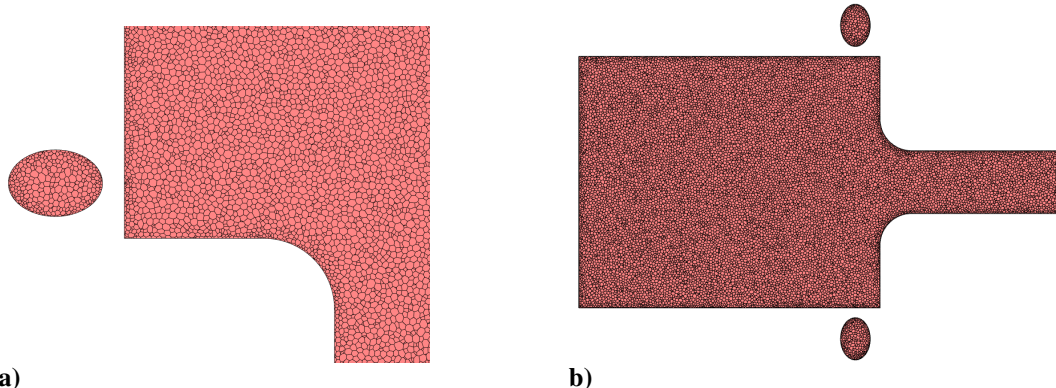


Fig. 2. Academic engine concept for a compact, tangentially-driven, cyclonic chamber.

Table 1. Geometric specifications

Parameter	Definition	Value	Units
Chamber Geometry			
L	Chamber length	6.10	cm
D_c	Chamber diameter	5.08	cm
L/D	Length-to-diameter ratio	1.2	
Swirl Injectors (aft-end)			
N_{inj}	Number of injectors	8	
D_{port}	Individual port diameter	0.605	cm
A_{port}	Injection area of individual port	1.1499	cm ²
A_{inj}	Total area of injection	9.1992	cm ²

**Fig. 3. Meshed geometry depicting a) zoomed view of the polyhedral elements and b) the polyhedral mesh elements inside the chamber.**

between the injectors and the chamber wall causes the mesh elements in this region to become highly skewed. To overcome this issue, a mesh consisting of tetrahedral elements is generated in a manner to minimize the skewness. The mesher that we use helps to evaluate the normalized mesh quality by yielding zero for a highly skewed element and unity for a perfect, unskewed element. Bearing this in mind while creating the mesh, the process is repeated until the normalized quality of the mesh returns a value above the minimum recommended threshold of 0.3.

To make further headway, we recognize that a tetrahedral mesh requires a relatively large number of elements for a given volume, thus increasing both the computation time and power requirements. As is customary, our tetrahedral mesh elements are converted into polyhedral elements using the reverse Cuthill-McKee algorithm. This step reduces computation time while improving convergence properties; in fact, it leads to simulation outcomes that are characteristic of a fully structured hexahedral mesh. Figure 3a provides a pictorial representation of the meshed geometry near the sidewall, where the inflation layers used to capture the wall boundary layers can be seen. The geometric mesh along the chamber surface and injector openings is depicted in Fig. 3b.

After mesh generation and the specification of boundary types, the mesh is imported into a robust finite volume solver. The simulation is then carried out using a steady, implicit, 3D, segregated solver. The computations are performed using a quasi-inviscid model that assumes laminar motion with inviscid slip walls. This is done for the purpose of facilitating the capture of stable and coherent cyclonic patterns that correspond to the available analytical solutions. More specifically, the use of a strictly inviscid computational model proves infeasible (and will always diverge) due to a well-known singularity affecting the tangential velocity at the centerline.

B. Conservation Equations

The conventional equations for conservation of mass and momentum are adapted for the flow in a cyclonic chamber. Using ρ and \mathbf{u} to represent the density and velocity, the fundamental equations that we solve are:

$$\frac{\partial \rho}{\partial t} + \nabla \cdot (\rho \mathbf{u}) = 0 \quad (\text{conservation of mass}) \quad (1)$$

$$\frac{\partial}{\partial t}(\rho\mathbf{u}) + \nabla \cdot (\rho\mathbf{u}\mathbf{u}) = -\nabla p + \nabla \cdot (\bar{\boldsymbol{\tau}}) + \rho\mathbf{g} + \mathbf{F} \quad (\text{conservation of momentum}) \quad (2)$$

where p stands for the static pressure, $\bar{\boldsymbol{\tau}}$ contains the stress tensor, $\rho\mathbf{g}$ symbolizes the gravitational body force, and \mathbf{F} consists of the external body force. In this framework, \mathbf{F} accounts for other model-dependent source terms such as porous media and user-defined sources [42]. The stress tensor, $\bar{\boldsymbol{\tau}}$, is given by

$$\bar{\boldsymbol{\tau}} = \mu \left[(\nabla \mathbf{u} + \nabla \mathbf{u}^T) - \frac{2}{3} (\nabla \cdot \mathbf{u}) \mathbf{I} \right] \quad (3)$$

where μ denotes the molecular viscosity, \mathbf{I} contains the unit tensor, and the second term on the right-hand-side captures the effect of volume dilation [42].

By taking advantage of the improved mesh and chamber configuration, the objective of the present study is to characterize all three components of the velocity, including the axial and radial components, which were omitted in previous work [39, 40]. We also aim at exploring the effect of changing the outlet diameter on the flowfield in a cyclonic chamber. To this end, the normalized outlet radius, β , is varied while keeping all other parameters fixed. The normalized outlet radius, β , is simply the ratio:

$$\beta = \frac{b}{a} \quad (4)$$

where b is the outlet radius and a represents the chamber radius. In our parametric trade analysis study, which is summarized in Table 2, the values of β are selected in a manner to coincide with their theoretical values for a cyclonic motion with multiple mantles, as derived by Vyas and Majdalani [5] for the complex-lamellar family of solutions. The same simulations can be as easily repeated using the multiple mantle locations associated with the Beltramian family of solutions found by Majdalani [3]. The baseline geometry is chosen to match the one used by Anderson et al. [28]. Since the flow remains incompressible, the total pressure is specified at the injector inlet point, outside the chamber, to be 100 psig with a static value of 98 psig, thus allowing for an inlet velocity of approximately 60 m/s. As for the outlet, it is set to be atmospheric. We find it essential to set the inlet boundary conditions on the pressure in order to mitigate the formation of multiple mantles. In other studies where velocity inlet conditions are used, multiple mantles are reported, including the work of Anderson et al. [28] and Sharma and Majdalani [40]. With the inlet condition being set as a pressure requirement, the robust SIMPLE algorithm is then used to couple the pressure with the velocity. In this process, the pressure is discretized according to the standard scheme and the momentum equation is discretized using a first-order upwind stencil. Other gradients are discretized using the Green-Gauss cell-based scheme. Finally, to promote a reasonable degree of precision, stringent convergence criteria are set. These ensure that the residuals remain consistently below a 10^{-6} tolerance level.

III. Results and Discussion

The primary aim of performing a numerical investigation of the bulk gaseous motion in a bidirectional vortex engine is to better understand the flow physics and identify its controlling parameters. In this vein, we proceed with a characterization of the axial and radial velocity components to complement previous results that mainly focused on the tangential component [40]. In addition, a parametric study is conducted to evaluate the effect of varying the outlet diameter on the flowfield. All velocities in this study are normalized by the average tangential injection speed, U .

In order to more effectively relate our computational results to existing analytical solutions, effort has been made to ensure that the CFD problem takes into account most of the parameters that are used in the analytical model, including, for example, the modified swirl number,

$$\sigma = \frac{a^2}{A_{\text{inj}}} \quad (5)$$

Table 2. Parametric study varying β

Case	1	2	3	4	5	6	7	8	9	10	11	12
β	0.3535	0.408	0.5	0.628	0.638	0.648	0.667	0.677	0.707	0.866	0.913	0.935

In the above, a denotes the radius of the chamber and A_{inj} refers to the total injection area. The second important parameter is often dubbed the off-swirl parameter as it gauges the absolute magnitude of axial and radial velocities relative to the tangential component, namely,

$$\kappa = \frac{1}{2\pi\sigma} \frac{a}{L} \quad (6)$$

where L represents the chamber length. Note that a lower value of κ implies larger tangential-to-radial or tangential-to-axial velocity ratios. In what follows, illustrative simulation results will be presented and these will correspond to our baseline Case 1 with $\beta = 0.5$ and $\kappa = 1/(2\pi \times 0.70132) \times (2.54/6.1) = 0.0945$, unless specified otherwise.

A. Velocity and Pressure Distributions

We begin with the tangential velocity distribution in Fig. 4a, where the radial variation of u_θ is illustrated at several discrete axial stations, starting at $z/L = 0.1$ near the headwall and ending with a value of 0.8 near the outlet. To be consistent with theory and tradition, such as Rankine's free vortex plots, the tangential velocity is normalized using the tangential speed, $U_w(z) = u_\theta(1, z)$, taken at the respective z/L locations. These results are shown side-by-side with the corresponding swirl velocity contour plots in Fig. 4b. Despite the elongated scale used in Fig. 4a, it may be seen that the axial variations of the swirl velocity are minimal. As one may expect, the maximum swirl velocity is slightly higher near the injection site at $z/L = 0.8$ and decreases as the headwall is approached. This can be more readily observed in the iso-velocity contours, which appear to be rather uniform along the length of the chamber, with a very minor decrease in the width of the $(u_\theta)_{\text{max}}$ isoband as z is increased. The corresponding behavior is reassuring as it helps to confirm the axial invariance assumption of the swirl velocity, which is often used at the basis of deriving cyclonic flow solutions. Furthermore, the existence of a forced vortex motion in the core region followed by a free vortex tail beyond the point of maximum u_θ can be ascertained from the swirl velocity plot depicted in Fig. 4a. Note that no values past $z/L = 0.8$ are shown to avoid nozzle entrance effects.

Next, we proceed to examine the pressure in Fig. 5, where it is normalized by its maximum radial value taken at $r = 1$. Although all cases adopt the same inlet pressure at their injectors entry point, this maximum pressure value at steady state will very slightly differ depending on the axial station within the chamber. Specifically, as we travel within the outer annular vortex, the normalizing pressure value taken at the sidewall will very slightly diminish as the headwall is approached. Here too, one may infer that the pressure gradient along the radius of the chamber remains

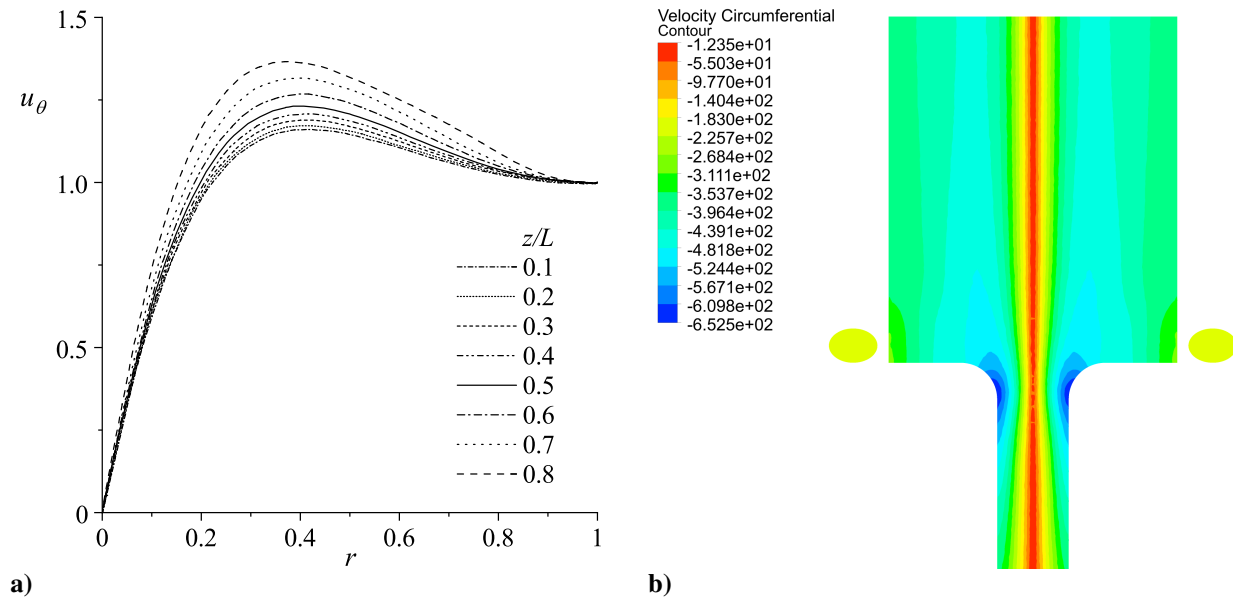


Fig. 4. We show a) the radial distribution of the normalized swirl velocity at eight z/L locations and b) swirl velocity contours [m/s] across a vertical r - z plane. We take $\beta = 0.5$ and $\kappa = 0.0945$ everywhere unless specified otherwise.

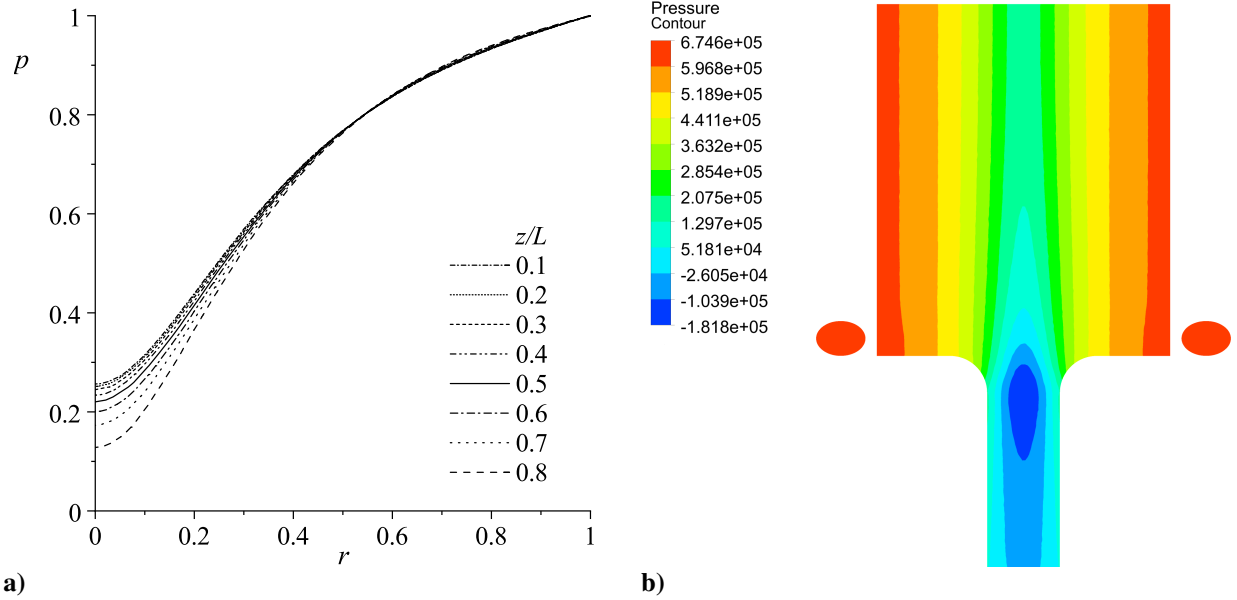


Fig. 5. We show a) the radial distribution of the normalized pressure at eight z/L locations and b) pressure contours [Pa] across a vertical r - z plane.

nearly independent of the axial distance, particularly in Fig. 5a, although minor deviations seem to occur near the axis of rotation. Naturally, if we consider the outer vortex region corresponding to $r \geq 0.5$, the pressure near the headwall must be slightly lower than the pressure near the injection site to force the upward convection of the incoming fluid. In contrast, the pressure within the inner vortex will slightly diminish in the direction of the outflow, namely, as z/L increases from 0.1 to 0.8. Nonetheless, these variations appear to be minimal at steady state if we are to travel axially along a constant r line. A similar trend may be inferred from the pressure contours of Fig. 5b, where the axial invariance of the pressure is fundamentally established across the entire domain. In fact, a similar pressure distribution is reported by Hoekstra et al. [10], Hu et al. [35], Murray et al. [38], and Majdalani and Chiaverini [1]. In short, the radial values of the pressure are found to be highest at the sidewall and lowest along the chamber axis, although axially, the sidewall pressure is very slightly lower at the headwall than the endwall, and the converse is true for the core pressure, which slightly decreases in the outflow direction.

As we turn our attention back to the axial velocity, its behavior is illustrated in Fig. 6a, where the radial distribution of u_z , normalized using the corresponding tangential speed at the wall, $U_w(z)$, is shown at eight different values of z/L . As usual, we start with a chained line at $z/L = 0.1$ and stop with a dashed line at a value of 0.8 near the outlet. The companion Fig. 6b displays the axial velocity contours across the chamber. It is evident from the plot that there exist two distinct regions that comprise an inner core and an outer, annular segment. Motion in the outer segment, which is positive upward until roughly $r \approx \beta = 0.5$, turns negative in the core region as the flow polarity switches and becomes downward.

The so-called updraft and downdraft regions, with two opposing axial polarities, are the reason a cyclonic motion is often dubbed bidirectional or bipolar. They are separated by a rotating but non-translating sheet or mantle, which is depicted using a solid line in Fig. 6b. This corresponds to the locus of $u_z = 0$, which evolves around a radius of $r \approx 0.504$, which is fairly close to the nozzle entrance radius β for this configuration. It can also be confirmed in Fig. 6 that the magnitude of $|u_z|$ increases in the core region as the fluid tries to leave the chamber. This behavior is further corroborated in the axial velocity contours of Fig. 11a, where the red color denotes incoming fluid moving upward, while the blue color marks the outgoing fluid on its way to exit the chamber.

Lastly, the radial velocity distribution in the chamber is explored in Fig. 7a, where symbols are used to represent different axial stations and thus help to illustrate the statistical scatter of the solution around its average value. Here, it can be seen that the average radial velocity is qualitatively similar to the theoretical form of u_r predicted by the family of analytical solutions described by Majdalani [3]. This includes the presence of a maximum absolute value for $|u_r|$ midway along the radius. Note that the solid line corresponds to a polynomial fit for the scatter plot and, as such, a

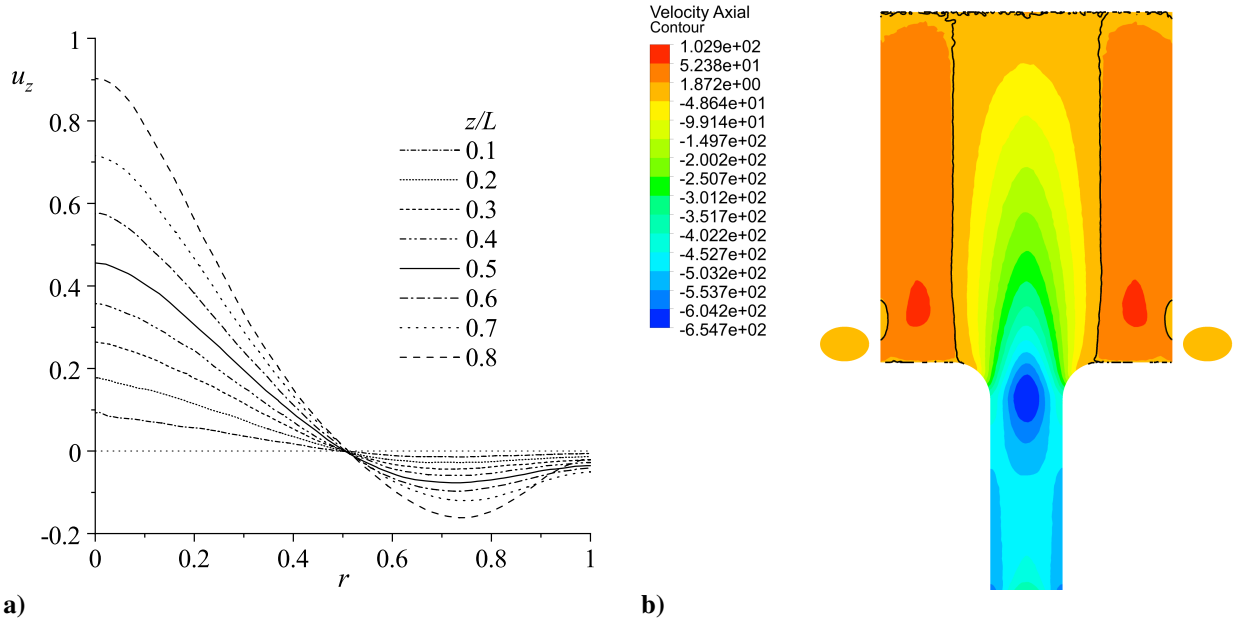


Fig. 6. We show a) the radial distribution of the normalized axial velocity at eight z/L locations and b) axial velocity contours [m/s] across a vertical r - z plane.

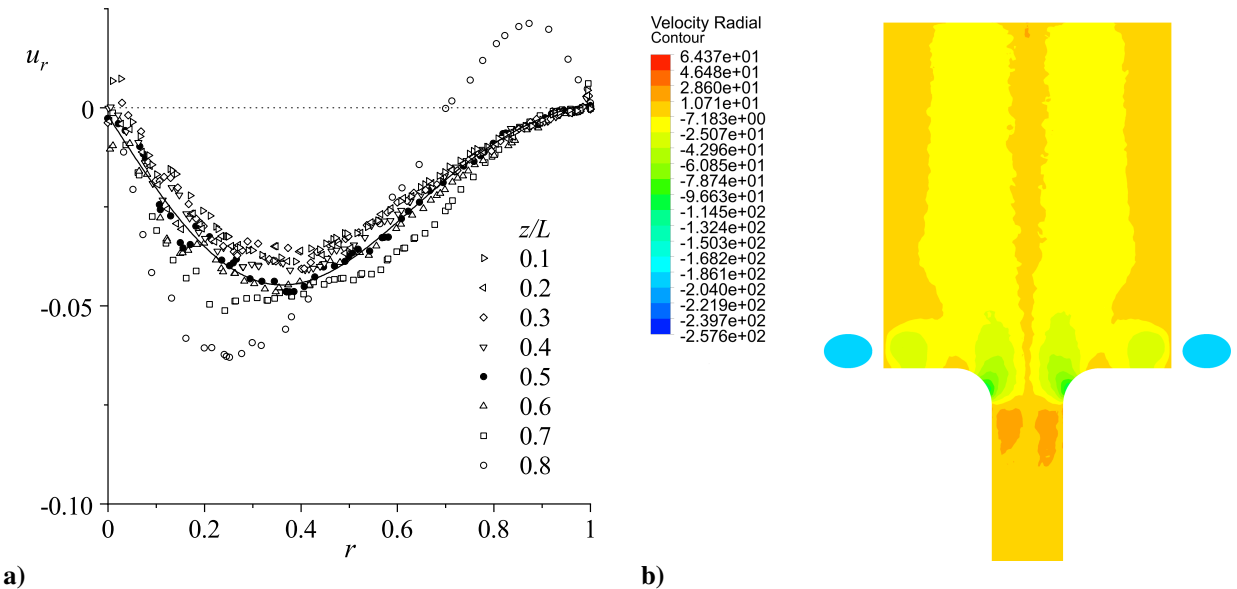


Fig. 7. We show a) the radial distribution of the radial velocity at eight z/L locations and b) radial velocity contours [m/s] across a vertical r - z plane. The solid line represents the data average.

rough representation of the average radial velocity obtained for this baseline case. The complementary radial velocity contours in Fig. 7b confirm these trends across the whole chamber where the axial invariance of u_r may be observed in the upper three quarters of the domain. In the bottom quarter length, the bulging and contraction of the contours may be attributed to the presence of finite injectors and a nozzle attachment in their vicinity, where a strong flow turning activity is prominent.

B. Effect of Outlet Sizing

Having showcased the capabilities of the numerically-computed flowfield at predicting the axial and radial velocities, we now proceed to vary the outlet diameter to study its effects on the axial velocity, the mantle location, the swirl velocity, and the pressure distribution. Naturally, with a fixed inlet pressure condition, varying the outlet diameter directly affects the mass flow rate leaving the chamber. The corresponding parametric study is therefore performed to better understand the influence of the normalized outlet radius, β , on the solution variables. Having already explored the flow characteristics using a benchmark $\beta = 0.5$, this value will serve as the control case for the remaining tests. As we proceed, the normalized outlet radius will be varied between 0.3535 and 0.935, as shown in Figs. 8–10, where the tangential velocity, pressure distribution, axial, and radial velocity plots are examined individually. We recall that the specific values of β are chosen because they correspond to the first theoretical investigation of multiple mantles

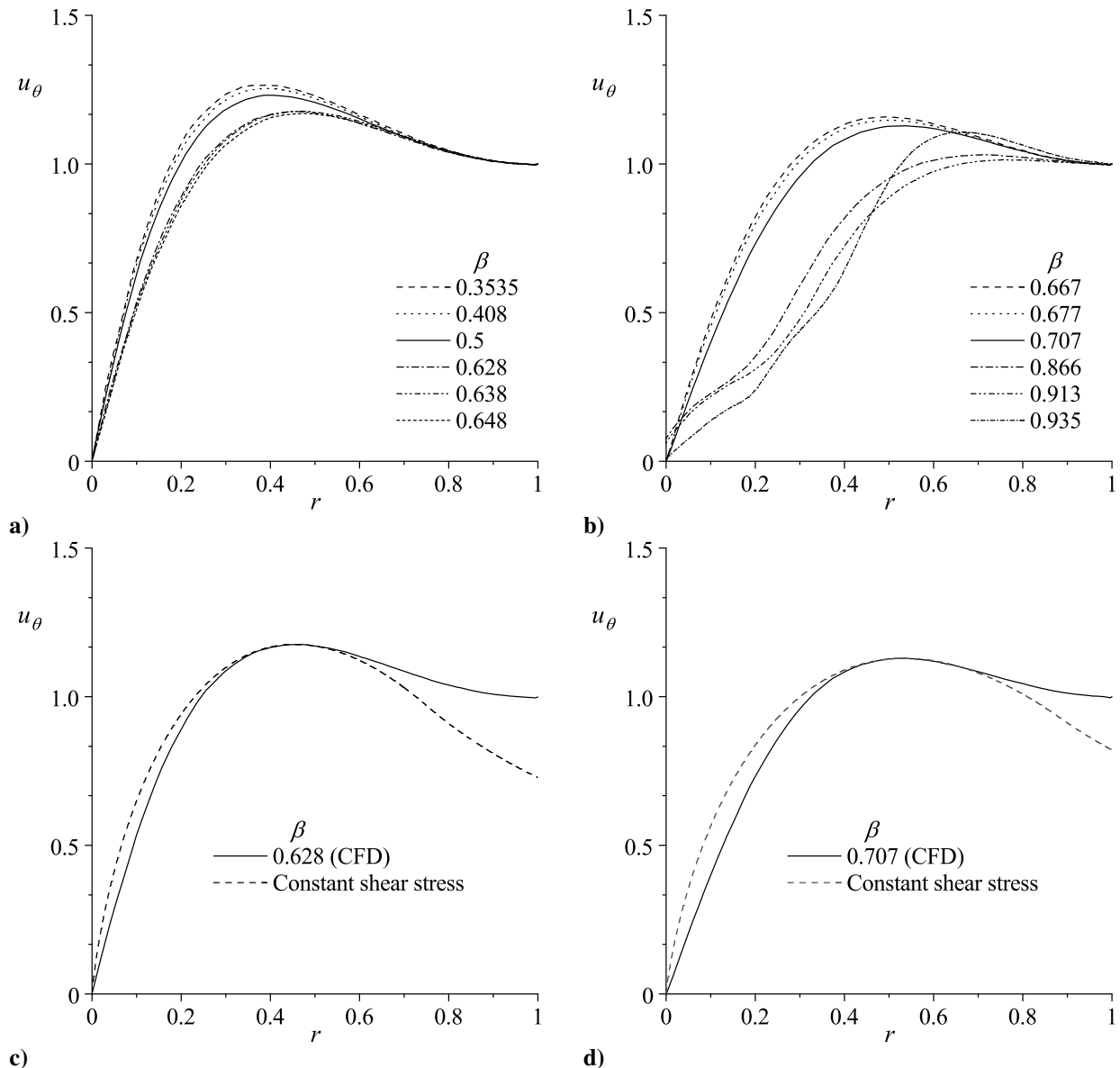


Fig. 8. Radial distribution of the swirl velocity at different values of β and $z/L = 0.5$ in Parts a) and b). Comparisons to the constant core shear model by Maicke and Majdalani [13] are provided for c) $\beta = 0.628$ and d) $\beta = 0.707$.

carried out by Vyas et al. [43], namely, where the locus of multiple mantles is identified and subsequently confirmed to a certain degree by the experimental measurements and CFD simulations of Anderson et al. [28] and Rom [45].

Forthwith, Fig. 8 illustrates the behavior of the quasi-inviscid form of the tangential velocity, normalized by $U_w(z)$, for various outlet diameters and a fixed station of $z/L = 0.5$. As expected, successive increments in the normalized outlet radius serve to decrease the peak swirl velocity in the chamber such that $(u_\theta)_{\max}$ is largest for $\beta = 0.353$. Rather interestingly, for $\beta > 0.707$, the peak swirl velocity moves consistently outwardly closer to the sidewall to compensate for an expanding outlet area. A similar pattern is reported by Talamantes and Maicke [39] in their preliminary computational results. The magnitude of the normalized u_θ near the sidewall also approaches a value of unity with successive increases in β , another trait that is apparent from the plots in Fig. 8.

Next, a pressure comparison is featured in Fig. 9 for the different cases of β and $z/L = 0.5$. As before, the pressure is normalized by its value taken at the wall. The first observation that we make in Fig. 9a is that the net pressure drop at the centerline increases as the outlet area is enlarged. Although the wall pressure is not shown, we find that, in all cases considered, the lowest pressure occurs at the centerline and the largest sidewall pressure is highest for the case with the smallest outlet area, or lowest β . Moreover, for $\beta \geq 0.707$ in Fig. 9b, the pressure near the centerline seems to flatten: the pressure gradient decreases, the peak pressure drops, and the pressure in the inner core plateaus to an essentially constant value. This behavior can be attributed to the presence of a recirculation zone that becomes more appreciable as the outlet area is enlarged. The reason for recirculation to occur will become apparent in the discussion below and will be associated with the emergence of a backflow region for $\beta \geq 0.707$. Except for the backflow effects, these trends seem to be comparable to those predicted theoretically by the Trkalian profile with no slip [3].

To further verify the trends exhibited by the CFD results, u_θ is compared to the tangential velocity profiles obtained using the constant core shear model developed by Maicke and Majdalani [13]. As the name implies, the latter assumes a constant shear stress to be dominant in the forced vortex region, which typically extends between the chamber axis and $r = r_{\max}$, where $u_\theta = (u_\theta)_{\max}$. It then transitions over the $r_{\max} \leq r < X$ interval into a free vortex motion that becomes prevalent for $r \geq X$. This comparison is showcased in Fig. 8c and Fig. 8d for $\beta = 0.628$ and $\beta = 0.707$, respectively. As one can infer from these plots, the profiles agree quite well with the constant core shear model for u_θ , namely,

$$\left(\frac{u_\theta}{U_w}\right) = \begin{cases} \frac{U_e}{U_w} \frac{r}{X^2} \left[1 - \ln\left(\frac{r^2}{X^2}\right) \right]; & r \leq X \\ \frac{U_e}{U_w} \frac{1}{r}; & r > X \end{cases} \quad (7)$$

where $X = r_{\max} \sqrt{e}$, $U_e = \frac{1}{2} e (u_\theta)_{\max} r_{\max} \approx 1.359 (u_\theta)_{\max} r_{\max}$, and r_{\max} denotes the locus of $(u_\theta)_{\max}$. In this

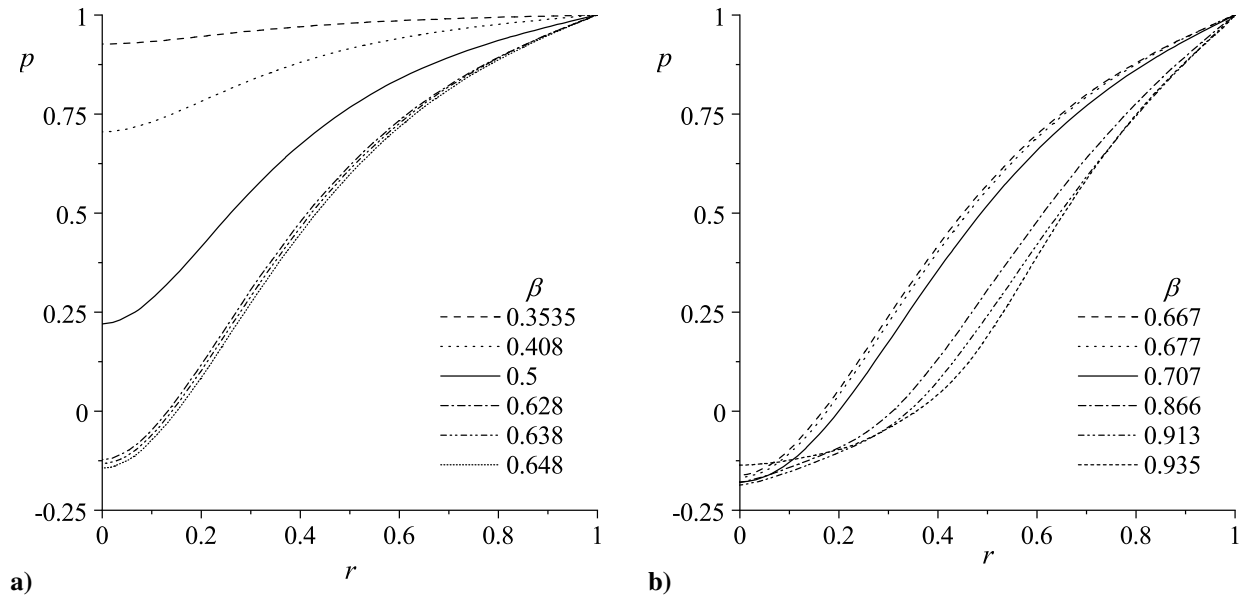


Fig. 9. Radial distribution of the pressure at different values of β and $z/L = 0.5$.

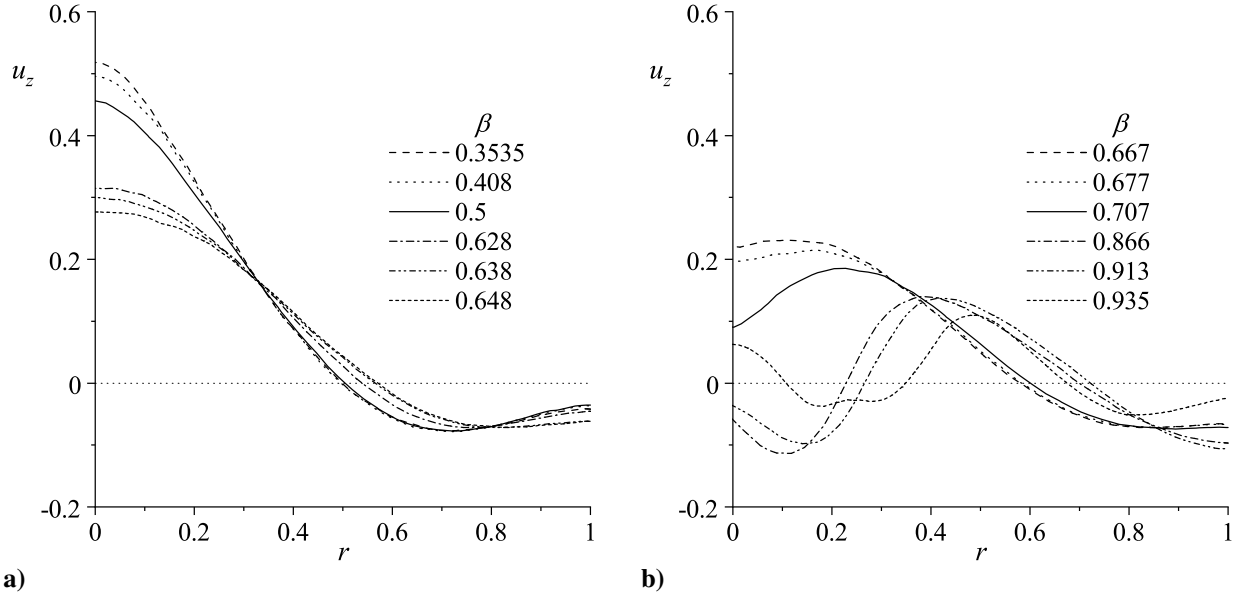


Fig. 10. Radial distribution of the axial velocity at different values of β and $z/L = 0.5$.

comparison, we find the dimensionless values of $X \approx 0.75$ and 0.88 with $r_{\max} = 0.455$ and 0.535 for $\beta = 0.628$ and 0.707 , respectively. As for the normalizing speeds associated with our numerical simulations, we compute $U_e/U_w = 0.728$ and 0.820 for the two cases in question.

Next, by switching to the axial velocity in Fig. 10, and its respective contours in Fig. 11, one can infer that the peak $|u_z(0, z)|$ at the centerline decreases monotonically as the outlet area is increased. This behavior is consistent with continuity and concurrent with the theoretical finding that a Beltrami profile with $\beta = 0.628$ will be accompanied by a higher axial velocity magnitude at the chamber outlet than the complex-lamellar profile with a larger $\beta = 0.707$. Such behavior is also corroborated in the axial velocity comparison presented by Majdalani [44] for the two types of profiles. Naturally, the magnitude of the axial velocity at the sidewall follows suit, and increases with β , as shown in Fig. 10. Note that for $\beta \geq 0.707$, flow recirculation can be surmised from the axial velocity distribution in Fig. 10b, and this is caused by the development of a backflow region that protrudes deeper into the chamber with successive expansions of the outlet diameter. More details on the backflow region and how to suppress it are provided further below.

It can be gleaned from the axial velocity contours in Fig. 11 that the mantle tends to adapt to the outlet size, particularly, by slightly repositioning itself to merge smoothly with the available outlet area. For outlet radii greater than $\beta = 0.707$, the mantle turns outwardly, as the flow approaches the outlet, to accommodate the larger outlet size. In contrast, for $\beta < 0.628$, it gradually turns inwardly while merging with the nozzle inlet. For in-between values of $0.628 \leq \beta \leq 0.707$, the diameter of the mantle remains nearly uniform as the flow exits the chamber.

It can also be remarked that as the exit radius is expanded in Fig. 11, a backflow region starts to form and move upstream into the chamber with successive increases in the outlet diameter. Specifically, the backflow remains secondary and confined within the nozzle section for $0.628 \leq \beta < 0.707$, i.e., with limited impact on the computed flowfield. However, for $\beta \geq 0.707$, the backflow region becomes gradually more prominent in size as it protrudes deeper into the chamber with successive increases in β . The development of a backflow region may be ascribed to the negative pressures that can occur in the core region, as predicted by Fig. 9.

Overall, the case with the largest $\beta = 0.935$ is found to be the most unstable as observed in Fig. 11. Therein, the mantle tries to form but the outlet radius appears to be excessively large for the mantle to realign itself with the available outlet area. Suppressing the backflow in this case, as in other such cases of internal backflow developments, requires geometric adjustments that will be briefly outlined next.

Before leaving this section, it may instructive to note that the present simulations, which are based on fixed pressure inlet conditions, do not give rise to multiple mantles. This leads us to speculate that the development of multiple mantles is not solely dependent on the outlet diameter, but rather influenced by other factors that remain unexplored.

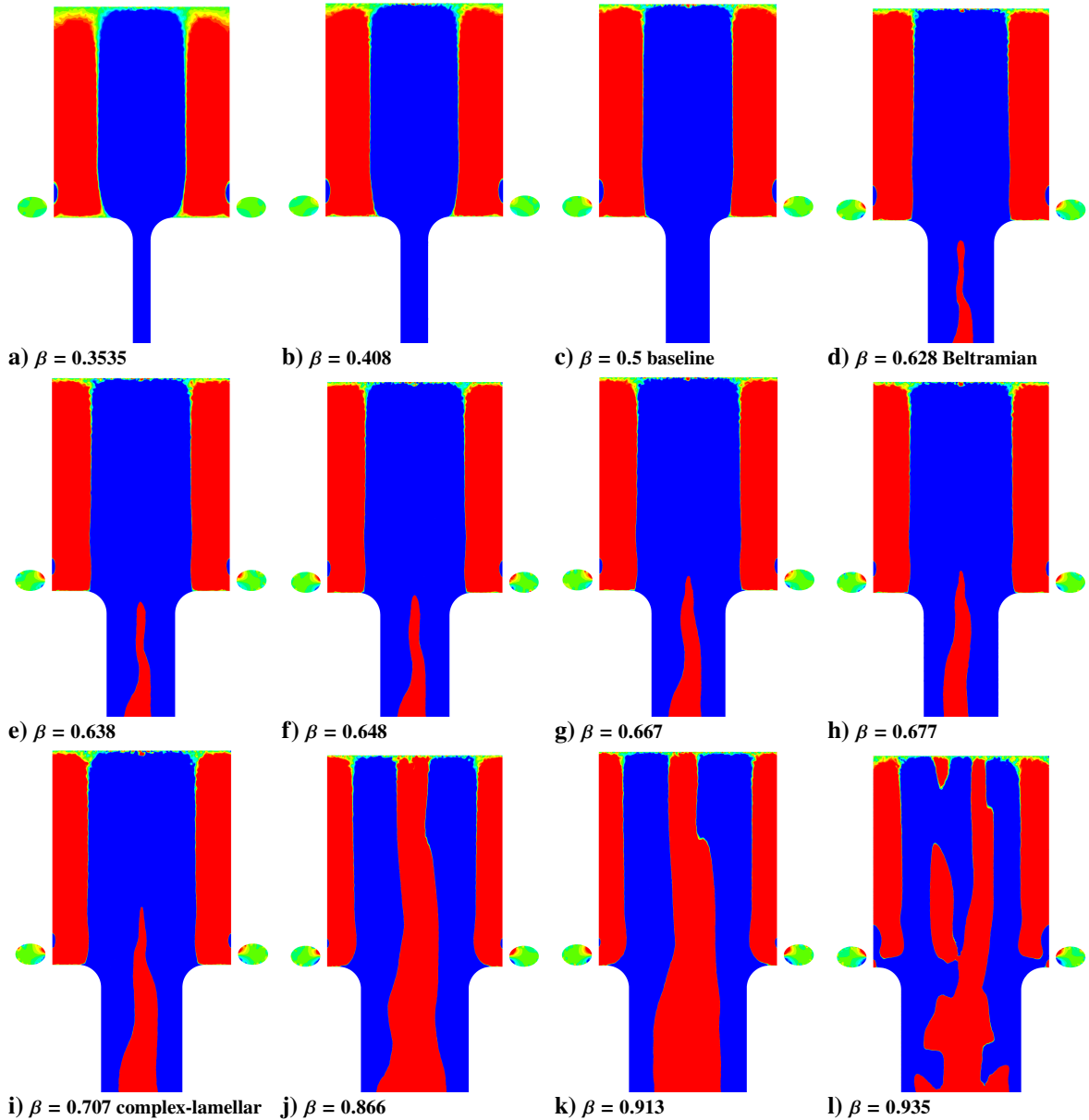


Fig. 11. Axial velocity contours that help to visualize the mantle for different cases of β .

These may include, for instance, the velocity-versus-pressure inlet conditions, the chamber aspect ratio, the nozzle diameter, the nozzle length, and the nozzle radius of curvature, as well as the operating conditions themselves. In what follows, the effect of the nozzle length and radius of curvature will be explored.

C. Effect of Outlet Transition

As we explore ways to prevent the backflow from forming, our initial step is to change the length of the nozzle extension. However, we find that increasing the nozzle length further can be problematic, as it can lead to unstable simulations. Conversely, reducing the nozzle length causes the backflow to penetrate deeper into the chamber. It thus appears that a finite range of nozzle lengths will produce a stable cyclonic flowfield for any $\beta \geq 0.628$.

In lieu of the nozzle length, we find that increasing R_N , the radius of curvature of the converging section of the nozzle, can be quite effective at suppressing the undesirable backflow. After several iterations, a value of 0.84 cm is found to be suitable for $\beta = 0.628$ and, similarly, a value of 1.04 cm is found to be adequate for $\beta = 0.707$.

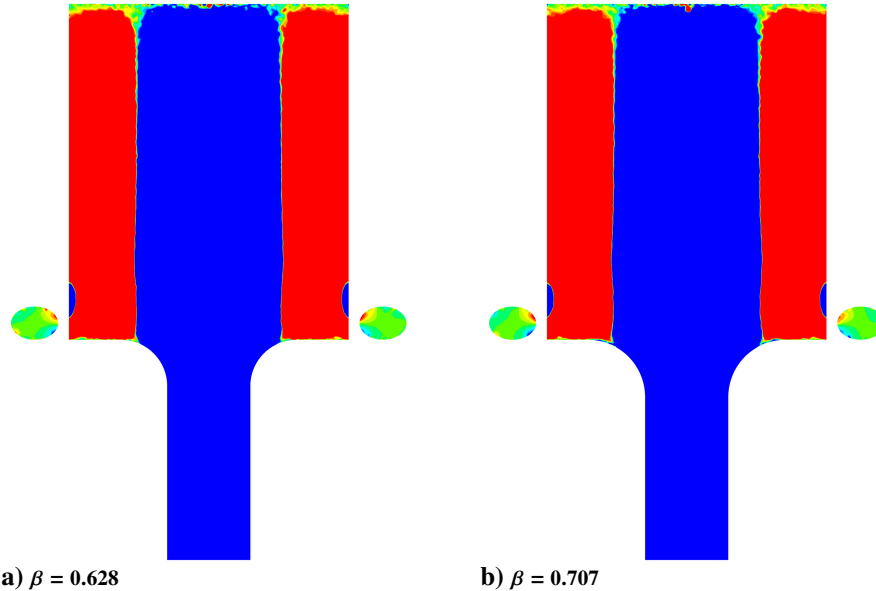


Fig. 12. Axial velocity contours that help to visualize the mantle for a) $\beta = 0.628$ and b) $\beta = 0.707$ after modifying the nozzle curvature in a manner to eliminate the backflow in Figs. 11d and 11i, respectively.

Recalling that the radius of the chamber is 2.54 cm, these curvatures translate into relative proportions of 0.33 and 0.41, respectively. Then noting that the normalized distances measured from the sidewall correspond to $(1 - 0.628) = 0.372$ and $(1 - 0.707) = 0.293$, we realize that the effective radii of curvature for both Beltrami and complex-lamellar configurations correspond to the same constant value of $0.33 \times 0.372 = 0.41 \times 0.293 = 0.12$. We can thus proceed to eliminate the backflow from all other cases using an effective radius of curvature that is deducible from a simple empirical relation, namely, $R_N = 0.12a/(1 - \beta)$.

The immediate effect of suppressing the backflow is illustrated in Fig. 12, where the simulations are repeated with a more optimal R_N , and used to produce the axial velocity contours for the two baseline cases of $\beta = 0.628$ and 0.707. On comparing Figs. 12a–12b with Fig. 11d and Fig. 11i, the elimination of recirculatory zones is evident. These contours also display quite distinctly the computationally-resolved mantle lines separating the outer (red) and inner (blue) regions. Although these mantles remain rather uniform, as predicted by theory, their numerically computed averages of 0.51 and 0.53 are slightly reduced due to the inward shifting that is required to accommodate a rounded nozzle entrance. These observations are reinforced in Fig. 13, where the radial distributions of the normalized u_z midway through the chamber are computed and displayed using our finite volume solver for the two nozzle configurations with and without backflow. The CFD results are also compared to available theoretical predictions that correspond in Fig. 13a to the Beltrami profile with $\beta = 0.628$ [3] and, in Fig. 13b, to the complex-lamellar profile with $\beta = 0.707$ [5]. As before, both CFD and theoretical predictions are normalized using the tangential velocity at the sidewall, $U_w(z)$. We note an overall agreement between theory and computation in the flow patterns, especially in comparing the theoretical profiles to their CFD predictions with no backflow. Nonetheless, the prediction of the mantle location by the CFD solution with backflow (dashed lines) is found to be closer to its theoretical value. Interestingly, in suppressing the backflow, an increased radius of curvature is required, thus leading to a smaller overall nozzle radius. In short, the effective radius for the nozzle configuration that entails a backflow remains larger and, therefore, closer to the theoretical value of the targeted β . We thus realize that by increasing the radius of curvature of the outlet nozzle, we constrict the outlet area and cause the mantle location to shift radially inwardly relative to its theoretically predicted value.

Finally, we compare the radial distribution of the normalized u_r in Fig. 14a and Fig. 14b for the two values of β , midway across the chamber, using the same CFD solutions that either allow or suppress the re-entrant backflow. Also included are the strictly inviscid analytical predictions based on the Beltrami and complex-lamellar models discussed previously [3, 5]. Despite the similarities in the spatial patterns displayed by these solutions, the computed radial velocities remain smaller in magnitude than their theoretical counterparts. Such differences may be attributed to the presence of viscous damping in the computational model, which seems to have a bearing on the radial velocity, especially that the latter cannot be affected by the imposed slip wall requirement.

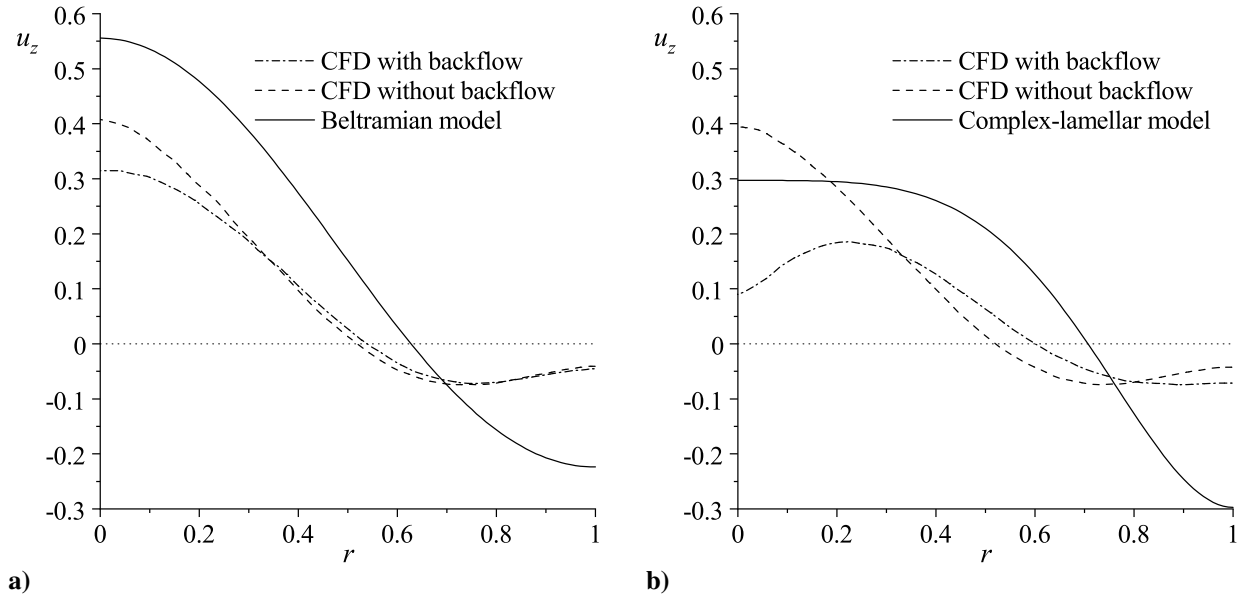


Fig. 13. Radial distribution of the normalized axial velocity for a) $\beta = 0.628$ and b) $\beta = 0.707$ at $z/L = 0.5$, both with and without backflow as per Figs. 11d and 11i and Figs. 12a and 12b, respectively. Also shown are the corresponding Beltrami and complex-lamellar profiles.

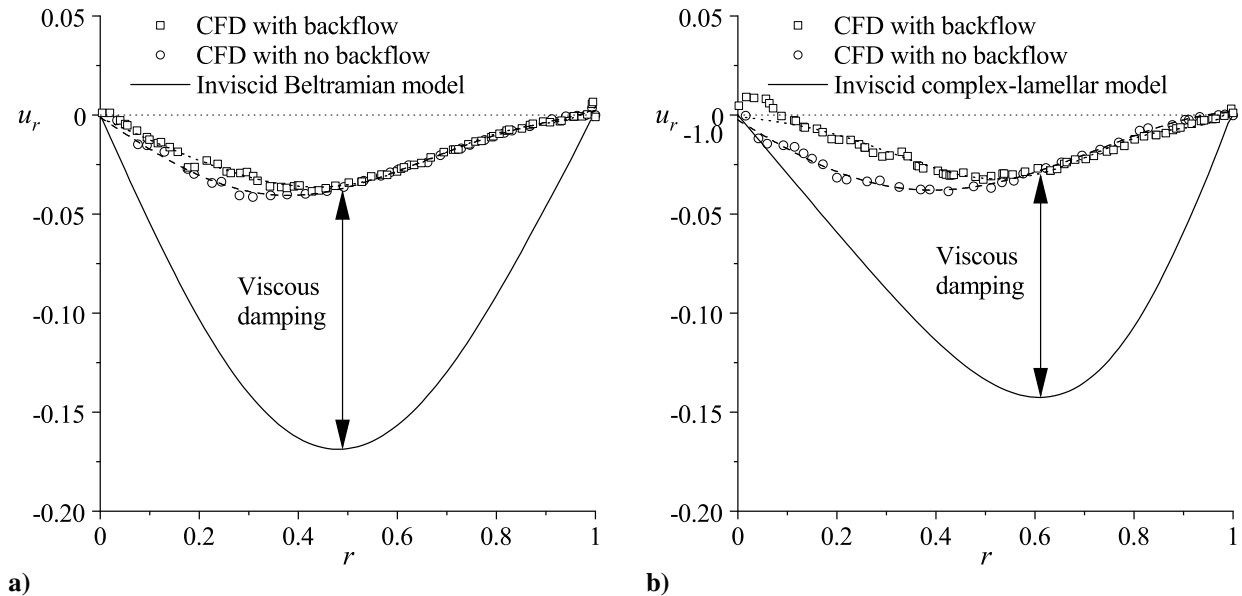


Fig. 14. Radial distribution of the normalized radial velocity for a) $\beta = 0.628$ and b) $\beta = 0.707$ at $z/L = 0.5$, both with and without backflow as per Figs. 11d and 11i and Figs. 12a and 12b, respectively. Also shown are the corresponding Beltrami and complex-lamellar profiles.

IV. Conclusion

Of the various computational studies that have undertaken the task of describing wall-bounded cyclonic flows, most have focused on industrial cyclone separators. Only few have been specific to the bidirectional vortex motion associated with a VCCWC chamber configuration. Furthermore, parametric studies related to outlet size variations

remain either scarce or inaccessible. By imposing slip-wall conditions in concert with a laminar flow solver, we show in this work that a judiciously constructed numerical model is capable of predicting the forced vortex behavior in the inner core region, as well as the free vortex motion in the outer region. These particular regions are well approximated analytically by a constant core shear stress model that entertains slip velocities along the walls and a constant shear stress around the core region. In a sense, it emulates to a certain degree the quasi-inviscid assumptions used in the numerical solver [13]. The work also confirms that a numerical model is somewhat effective at characterizing the pressure distribution as well as other flow variables of interest. For example, the parametric trade analysis conducted so far suggests that increasing the normalized outlet radius, β , can have an appreciable impact on the swirl velocity, axial velocity, mantle location, and pressure distribution throughout the chamber. In fact, as the outlet area is increased, the peak tangential velocity is reduced and drawn radially outwardly. The pressure drop along the chamber axis is also increased until $\beta = 0.707$, beyond which the pressure curves start to asymptote in the inner core region. The same can be said of the mantle location, which seems to adapt itself to the expanding outlet diameter, until it can no longer attach itself to the nozzle inlet circumference. Incidentally, when the outlet diameter becomes sufficiently large, a backflow region seems to evolve in the nozzle area and then creep upstream into the chamber with successive increases in β . Pursuant to a cursory investigation, the backflow formation is found to be quite sensitive to geometric changes, especially in the nozzle region. To suppress this recirculatory zone, we find it useful to increase the radius of curvature at the nozzle entrance region to the extent of reducing the final outlet diameter. In this process, we identify a nozzle inlet curvature, $R_N = 0.12a/(1 - \beta)$, that will prevent the backflow from occurring. Unsurprisingly, increasing this curvature eliminates the backflow but causes the mantles to shift radially inwardly while compelling the corresponding axial velocities to increase near the centerline, as in the classical case of *vena contracta*. Naturally, any area contraction must be accompanied by an increase in the axial velocity magnitude, which is necessary to evacuate the same amount of fluid across a narrower passage. This trend is further reflected in the higher axial velocities observed in both CFD and analytical models of the Beltrami motion with $\beta = 0.628$, i.e., when gauged against the computational and complex-lamellar solutions with a larger $\beta = 0.707$. Finally, as far as the development of multiple mantles is concerned, we initially speculate that multiple flow passes may be triggered by the narrowing of the outlet diameter. Nonetheless, despite the pre-selection of outlet diameters that are guided by the theoretical solutions of Vyas et al. [43], we are unable to replicate any of the multiple mantle combinations reported numerically, nor those observed experimentally in the works of Anderson et al. [28], Rom [45], Sharma and Majdalani [40], and others. Instead, we find that the imposition of pressure rather than velocity inlet conditions in the solver will effectively mitigate the development of multiple mantles. In future work, we hope to conduct a wider range of parametric trade permutations to make it possible to determine the threshold values of the principal parameters that control the onset, precession, and breakdown of wall-bounded cyclonic flows under both laminar and turbulent conditions.

Acknowledgements

This work was supported partly by the National Science Foundation and partly by the Hugh and Loeda Francis Chair of Excellence, Department of Aerospace Engineering, Auburn University. The authors are particularly thankful to Langston L. Williams for his valuable assistance. We are also deeply indebted to Dr. Martin J. Chiaverini, Director of Propulsion Systems at Sierra Nevada Corporation, for numerous technical exchanges and for his unwavering support of our cyclonic flow investigations.

References

- [1] Majdalani, J. and Chiaverini, M. J., "Characterization of GO2–GH2 Simulations of a Miniature Vortex Combustion Cold-Wall Chamber," *Journal of Propulsion and Power*, Vol. 33, No. 2, March 2017, pp. 387–397. doi:[10.2514/1.b36277](https://doi.org/10.2514/1.b36277).
- [2] Penner, S. S., "Elementary Considerations of the Fluid Mechanics of Tornadoes and Hurricanes," *Acta Astronautica*, Vol. 17, 1971, pp. 351–362.
- [3] Majdalani, J., "Helical Solutions of the Bidirectional Vortex in a Cylindrical Cyclone: Beltrami and Trkalian Motions," *Fluid Dynamics Research*, Vol. 44, No. 6, October 2012, pp. 065506. doi:[10.1088/0169-5983/44/6/065506](https://doi.org/10.1088/0169-5983/44/6/065506).
- [4] Majdalani, J., "Unified Framework for Modeling Swirl Dominated Helical Motions," *50th AIAA/ASME/SAE/ASEE Joint Propulsion Conference*, AIAA Paper 2014-3677, July 2014. doi:[10.2514/6.2014-3677](https://doi.org/10.2514/6.2014-3677).
- [5] Vyas, A. B. and Majdalani, J., "Exact Solution of the Bidirectional Vortex," *AIAA Journal*, Vol. 44, No. 10, October 2006,

pp. 2208–2216. doi:[10.2514/1.14872](https://doi.org/10.2514/1.14872).

[6] ter Linden, A. J., “Investigations into Cyclone Dust Collectors,” *Proceedings of the Institution of Mechanical Engineers*, Vol. 160, No. 1, June 1949, pp. 233–251. doi:[10.1243/pime_proc_1949_160_025_02](https://doi.org/10.1243/pime_proc_1949_160_025_02).

[7] Bloor, M. I. G. and Ingham, D. B., “The Flow in Industrial Cyclones,” *Journal of Fluid Mechanics*, Vol. 178, No. 1, May 1987, pp. 507. doi:[10.1017/s0022112087001344](https://doi.org/10.1017/s0022112087001344).

[8] Hsieh, K. T. and Rajamani, R. K., “Mathematical Model of the Hydrocyclone Based on Physics of Fluid Flow,” *AIChE Journal*, Vol. 37, No. 5, May 1991, pp. 735–746. doi:[10.1002/aic.690370511](https://doi.org/10.1002/aic.690370511).

[9] Monredon, T., Hsieh, K., and Rajamani, R., “Fluid Flow Model of the Hydrocyclone: An Investigation of Device Dimensions,” *International Journal of Mineral Processing*, Vol. 35, No. 1-2, June 1992, pp. 65–83. doi:[10.1016/0301-7516\(92\)90005-h](https://doi.org/10.1016/0301-7516(92)90005-h).

[10] Hoekstra, A., Derkxen, J., and Akker, H. V. D., “An Experimental and Numerical Study of Turbulent Swirling Flow in Gas Cyclones,” *Chemical Engineering Science*, Vol. 54, No. 13-14, July 1999, pp. 2055–2065. doi:[10.1016/s0009-2509\(98\)00373-x](https://doi.org/10.1016/s0009-2509(98)00373-x).

[11] Majdalani, J. and Rienstra, S. W., “On the Bidirectional Vortex and Other Similarity Solutions in Spherical Coordinates,” *Zeitschrift für angewandte Mathematik und Physik*, Vol. 58, No. 2, September 2006, pp. 289–308. doi:[10.1007/s00033-006-5058-y](https://doi.org/10.1007/s00033-006-5058-y).

[12] Majdalani, J. and Chiaverini, M. J., “On Steady Rotational Cyclonic Flows: The Viscous Bidirectional Vortex,” *Physics of Fluids*, Vol. 21, No. 10, October 2009, pp. 103603. doi:[10.1063/1.3247186](https://doi.org/10.1063/1.3247186).

[13] Maicke, B. A. and Majdalani, J., “A Constant Shear Stress Core Flow Model of the Bidirectional Vortex,” *Proceedings of the Royal Society A: Mathematical, Physical and Engineering Sciences*, Vol. 465, No. 2103, March 2009, pp. 915–935. doi:[10.1098/rspa.2008.0342](https://doi.org/10.1098/rspa.2008.0342).

[14] Batterson, J. W. and Majdalani, J., “Sidewall Boundary Layers of the Bidirectional Vortex,” *Journal of Propulsion and Power*, Vol. 26, No. 1, January 2010, pp. 102–112. doi:[10.2514/1.40442](https://doi.org/10.2514/1.40442).

[15] Batterson, J. and Majdalani, J., “On the Viscous Bidirectional Vortex. Part 1: Linear Beltrami Motion,” *46th AIAA/ASME/SAE/AIAA Joint Propulsion Conference and Exhibit*, AIAA Paper 2010-6763, July 2010. doi:[10.2514/6.2010-6763](https://doi.org/10.2514/6.2010-6763).

[16] Batterson, J. and Majdalani, J., “On the Viscous Bidirectional Vortex. Part 2: Nonlinear Beltrami Motion,” *46th AIAA/ASME/SAE/AIAA Joint Propulsion Conference and Exhibit*, AIAA Paper 2010-6764, July 2010. doi:[10.2514/6.2010-6764](https://doi.org/10.2514/6.2010-6764).

[17] Akiki, G. and Majdalani, J., “On the Bidirectional Vortex with Arbitrary Endwall Velocity,” *46th AIAA/ASME/SAE/AIAA Joint Propulsion Conference and Exhibit*, AIAA Paper 2010-6652, July 2010. doi:[10.2514/6.2010-6652](https://doi.org/10.2514/6.2010-6652).

[18] Akiki, G., *On the Bidirectional Vortex Engine Flowfield with Arbitrary Endwall Injection*, Master’s thesis, University of Tennessee, Knoxville, August 2011.

[19] Maicke, B. and Majdalani, J., “On The Compressible Bidirectional Vortex,” *44th AIAA/ASME/SAE/AIAA Joint Propulsion Conference and Exhibit*, AIAA Paper 2008-4834, July 2008. doi:[10.2514/6.2008-4834](https://doi.org/10.2514/6.2008-4834).

[20] Maicke, B. A., Cecil, O. M., and Majdalani, J., “On the Compressible Bidirectional Vortex in a Cyclonically Driven Trkalian Flow Field,” *Journal of Fluid Mechanics*, Vol. 823, June 2017, pp. 755–786. doi:[10.1017/jfm.2017.310](https://doi.org/10.1017/jfm.2017.310).

[21] Fleischmann, J. and Majdalani, J., “Complex Lamellar Helical Solution for Cyclonically Driven Hybrid Rocket Engines,” *53rd AIAA Aerospace Sciences Meeting*, AIAA Paper 2015-0372, January 2015. doi:[10.2514/6.2015-0372](https://doi.org/10.2514/6.2015-0372).

[22] Marquardt, T. and Majdalani, J., “Beltrami Solution for Cyclonically Driven Hybrid Rocket Engines,” *53rd AIAA/SAE/AIAA Joint Propulsion Conference*, AIAA Paper 2017-4638, July 2017. doi:[10.2514/6.2017-4638](https://doi.org/10.2514/6.2017-4638).

[23] Barber, T. A., Cecil, O. M., and Majdalani, J., “Complex-Lamellar Cyclonic Vortex in a Cylindrical Chamber with a Hollow Core,” *51st AIAA/SAE/AIAA Joint Propulsion Conference*, AIAA Paper 2015-3848, July 2015. doi:[10.2514/6.2015-3848](https://doi.org/10.2514/6.2015-3848).

[24] Knuth, W., Gramer, D., Chiaverini, M., Sauer, J., Whitesides, R., and Dill, R., “Preliminary CFD Analysis of the Vortex Hybrid Rocket Chamber and Nozzle Flow Field,” *34th AIAA/ASME/SAE/AIAA Joint Propulsion Conference and Exhibit*, AIAA Paper 1998-3351, July 1998. doi:[10.2514/6.1998-3351](https://doi.org/10.2514/6.1998-3351).

[25] Knuth, W. H., Chiaverini, M. J., Sauer, J. A., and Gramer, D. J., "Solid-Fuel Regression Rate Behavior of Vortex Hybrid Rocket Engines," *Journal of Propulsion and Power*, Vol. 18, No. 3, May 2002, pp. 600–609. doi:[10.2514/2.5974](https://doi.org/10.2514/2.5974).

[26] Chiaverini, M., Malecki, M., Sauer, J., Knuth, W., and Hall, C., "Vortex Combustion Chamber Development For Future Liquid Rocket Engine Applications," *38th AIAA/ASME/SAE/ASEE Joint Propulsion Conference and Exhibit*, AIAA Paper 2002-4149, July 2002. doi:[10.2514/6.2002-4149](https://doi.org/10.2514/6.2002-4149).

[27] Chiaverini, M., Malecki, M., Sauer, J., Knuth, W., and Majdalani, J., "Vortex Thrust Chamber Testing and Analysis for O2-H2 Propulsion Applications," *39th AIAA/ASME/SAE/ASEE Joint Propulsion Conference and Exhibit*, AIAA Paper 2003-4473, July 2003. doi:[10.2514/6.2003-4473](https://doi.org/10.2514/6.2003-4473).

[28] Anderson, M., Valenzuela, R., Bonazza, R., Chiaverini, M., and Rom, C., "Vortex Chamber Flow Field Characterization for Gelled Propellant Combustor Applications," *39th AIAA/ASME/SAE/ASEE Joint Propulsion Conference and Exhibit*, AIAA Paper 2003-4474, July 2003. doi:[10.2514/6.2003-4474](https://doi.org/10.2514/6.2003-4474).

[29] Maicke, B. A. and Majdalani, J., "Inviscid Models of Cyclonically Driven Internal Flows," *International Journal of Energetic Materials and Chemical Propulsion*, Vol. 15, No. 4, 2016, pp. 305–324. doi:[10.1615/intjenergeticmaterialschemprop.2016016511](https://doi.org/10.1615/intjenergeticmaterialschemprop.2016016511).

[30] Boysan, F., Ayers, W. H., and Swithenbank, J., "A Fundamental Mathematical Modelling Approach to Cyclone Design," *Trans. Inst. Chem. Eng. Transactions of the Institution of Chemical Engineers, London*, Vol. 60, No. 4, 1982, pp. 222–230.

[31] Concha, F., Barrientos, A., Munoz, L., Bustamante, O., and Castro, O., "A Phenomenological Model of a Hydrocyclone," *International Conference on Hydrocyclones 96 MEP Ltd.*, April 1996, pp. 63–82.

[32] Derksen, J. J. and den Akker, H. E. A. V., "Simulation of Vortex Core Precession in a Reverse-Flow Cyclone," *AICHE Journal*, Vol. 46, No. 7, July 2000, pp. 1317–1331. doi:[10.1002/aic.690460706](https://doi.org/10.1002/aic.690460706).

[33] Derksen, J. J., "Separation Performance Predictions of a Stairmand High-Efficiency Cyclone," *AICHE Journal*, Vol. 49, No. 6, June 2003, pp. 1359–1371. doi:[10.1002/aic.690490603](https://doi.org/10.1002/aic.690490603).

[34] Derksen, J. J., van den Akker, H. E. A., and Sundaresan, S., "Two-Way Coupled Large-Eddy Simulations of the Gas-Solid Flow in Cyclone Separators," *AICHE Journal*, Vol. 54, No. 4, 2008, pp. 872–885. doi:[10.1002/aic.11418](https://doi.org/10.1002/aic.11418).

[35] Hu, L. Y., Zhou, L. X., Zhang, J., and Shi, M. X., "Studies on Strongly Swirling Flows in the Full Space of a Volute Cyclone Separator," *AICHE Journal*, Vol. 51, No. 3, 2005, pp. 740–749. doi:[10.1002/aic.10354](https://doi.org/10.1002/aic.10354).

[36] Cortes, C. and Gil, A., "Modeling the Gas and Particle Flow Inside Cyclone Separators," *Progress in Energy and Combustion Science*, Vol. 33, No. 5, October 2007, pp. 409–452. doi:[10.1016/j.pecs.2007.02.001](https://doi.org/10.1016/j.pecs.2007.02.001).

[37] Fang, D. and Majdalani, J., "Simulation of the Cold-Wall Swirl Driven Combustion Chamber," *39th AIAA/ASME/SAE/ASEE Joint Propulsion Conference and Exhibit*, AIAA Paper 2003-5055, July 2003. doi:[10.2514/6.2003-5055](https://doi.org/10.2514/6.2003-5055).

[38] Murray, A. L., Gudgen, A. J., Chiaverini, M. J., Sauer, J. A., and Knuth, W. H., "Numerical Code Development for Simulating Gel Propellant Combustion Processes," *JANNAF*, May 2004.

[39] Talamantes, G. and Maicke, B. A., "Parametric Study of the Bidirectional Vortex through Outlet Variation," *53rd AIAA/SAE/ASEE Joint Propulsion Conference*, AIAA Paper 2017-4753, July 2017. doi:[10.2514/6.2017-4753](https://doi.org/10.2514/6.2017-4753).

[40] Sharma, G. and Majdalani, J., "Characterization of the Cyclonic Flowfield in a Swirl Driven Combustion Chamber," *53rd AIAA/SAE/ASEE Joint Propulsion Conference*, AIAA Paper 2017-4667, July 2017. doi:[10.2514/6.2017-4667](https://doi.org/10.2514/6.2017-4667).

[41] Maicke, B. A. and Talamantes, G., "Numerical Investigation of Injection Variation in the Bidirectional Vortex," *AIAA Journal*, Vol. 55, No. 8, June 2017, pp. 2544–2554. doi:[10.2514/1.j055807](https://doi.org/10.2514/1.j055807).

[42] ANSYS, "Fluent, Release 2020 R1, Version 18.1," 2020.

[43] Vyas, A., Majdalani, J., and Chiaverini, M., "The Bidirectional Vortex. Part 3: Multiple Solutions," *39th AIAA/ASME/SAE/ASEE Joint Propulsion Conference and Exhibit*, AIAA Paper 2003-5054, July 2003. doi:[10.2514/6.2003-5054](https://doi.org/10.2514/6.2003-5054).

[44] Majdalani, J., "Exact Eulerian Solutions of the Cylindrical Bidirectional Vortex," *45th AIAA/ASME/SAE/ASEE Joint Propulsion Conference and Exhibit*, AIAA Paper 2009-5307, August 2009. doi:[10.2514/6.2009-5307](https://doi.org/10.2514/6.2009-5307).

[45] Rom, C. J., *Flow Field and Near Nozzle Fuel Spray Characterizations for a Cold Flowing Vortex Engine*, Master's thesis, University of Wisconsin, Madison, May 2006.